Mikada, H., Moore, G.F., Taira, A., Becker, K., Moore, J.C., and Klaus, A. (Eds.)
Proceedings of the Ocean Drilling Program, Scientific Results Volume 190/196

7. Microstructural Variations in Sediments from the Toe of the Nankai Accretionary Prism: Results of Scanning Electron Microscope Analysis[1]

E. Blanche Sunderland[2] and Julia K. Morgan[2]

ABSTRACT

Scanning electron microscope analyses of sediment samples collected from the frontal portion of the Nankai accretionary prism and Shikoku Basin during Ocean Drilling Program Leg 190 show systematic changes in clay microstructure and microfabric that correlate with depth, lithology, sediment deformation, and changing physical properties. Heterogeneous, open sediment textures found in the shallower lithologies, such as the upper Shikoku Basin facies, are characterized by random distributions of coarse particle aggregates and fine-grained clay minerals distributed throughout the matrix. The degree of clay mineral preferred orientation (CPO) generally increases with depth and adjacent to deformation structures but is retarded in an anomalous zone of high porosities at the reference Site 1173. Clay microstructures in and below the anomalous zone are very similar and provide little evidence that clays serve as the cementing agent. Deeper sediments, including most of the lower Shikoku Basin facies, exhibit more homogeneous distributions of dispersed and uniformly sized clay particles and commonly exhibit a high degree of CPO. The transition in texture appears to occur at the protodécollement horizon at the reference Site 1173 and slightly shallower in the section within the protothrust zone. The coincidence of this transition with noticeable downhole decreases in smectite abundance and compressional wave velocity (V_P) at Site 1173

[1]Sunderland, E.B., and Morgan, J.K., 2003. Microstructural variations in sediments from the toe of the Nankai accretionary prism: results of scanning electron microscope analysis. *In* Mikada, H., Moore, G.F., Taira, A., Becker, K., Moore, J.C., and Klaus, A. (Eds.), *Proc. ODP, Sci. Results,* 190/196, 1–27 [Online]. Available from World Wide Web: <http://www-odp.tamu.edu/publications/190196SR/VOLUME/CHAPTERS/212.PDF>. [Cited YYYY-MM-DD]
[2]Department of Earth Science, Rice University, 6100 Main Street, MS 126, Houston TX 77005, USA.
blanche@rice.edu

Initial receipt: 19 November 2002
Acceptance: 24 July 2003
Web publication: 15 April 2004
Ms 190SR-212

highlight an important diagenetic boundary that may help to localize slip along the accretionary décollement as it propagates seaward.

INTRODUCTION

Drill cores recovered from the Shikoku Basin (seaward of the Nankai accretionary prism) during Deep Sea Drilling Project (DSDP) Leg 87 and Ocean Drilling Program (ODP) Leg 190 reveal unusual downhole trends in key physical properties, most notably porosity and density. Unlike typical normally consolidated marine sediments, which show decreasing porosity with depth (e.g., Athy, 1930; Hamilton, 1976), strata in the upper Shikoku Basin (USB) unit exhibit anomalously high porosities, up to 10%–15% higher than predicted for their depths (Bray and Karig, 1986; Shipboard Scientific Party, 2001a). Porosities in the surrounding stratigraphic units follow more typical depth trends. In addition, porosities within the correlative USB unit in the accretionary prism, at Sites 1174 and 808, lie much closer to typical porosity depth trends (Shipboard Scientific Party, 1991; Shipboard Scientific Party, 2001b), denoting changes that accompany sediment accretion (e.g., Bray and Karig, 1985). The origin of these anomalous physical properties in front of the prism is a subject of debate. They may result from localized overpressures in the USB unit (e.g., Bray and Karig, 1986, 1988) or, alternatively, from intergranular cementation that supports the sediment matrix against consolidation (e.g., Karig, 1993; Moore, Taira, Klaus, et al., 2001). The downhole and downdip transitions in physical properties reflect major changes in mechanical behavior that may govern the types and distributions of deformation structures that develop in the accretionary prism.

Here, we examine additional evidence to determine the origin of the anomalous physical properties in the nontectonically deformed USB sediments. Following a review of new shipboard data collected during Leg 190 that bear on the interpretation of the physical property trends, we present scanning electron microscopy (SEM) analyses of sediment microstructure and microfabrics in and adjacent to the USB. These observations confirm the anomalous character of sediments in the USB at Site 1173 and demonstrate systematic downhole and downdip changes in microfabric, lithology, and corresponding physical properties. Comparison of these results with grain size, mineralogy, and pore fluid chemistry data point to the combined effects of diagenetic and mechanical changes as the sediments are buried and tectonically loaded. These spatial and temporal variations in properties and microfabric may play an important role in localization of deformation in the prism, including the positioning of the basal décollement fault.

GEOLOGIC SETTING

The Nankai accretionary prism lies off the south coast of Shikoku Island, Japan, a result of northwest convergence between the Philippine Sea plate and the Eurasian plate (Karig and Angevine, 1986; Seno et al., 1993). During Leg 190, the prism was cored at several locations along a transect offshore of Muroto Peninsula, for purposes of investigating the structural evolution and fluid flow of the prism (Moore, Taira, Klaus, et al., 2001; Moore et al., 2001). Site 1173 was drilled seaward of the prism, as a reference site in the Shikoku Basin. Site 1174 penetrates the

toe of the Nankai prism, in the protothrust zone (PTZ) ~10 km landward of the deformation front. A third site, Site 808, drilled during ODP Leg 131 through the frontal thrust, 2 km landward of Site 1174, completes the frontal Muroto transect, but will not be considered here.

The stratigraphic section along the Muroto transect is dominated by hemipelagic sediments of the Shikoku Basin facies (Moore, Taira, Klaus, et al., 2001). The USB facies is distinguished from the lower Shikoku Basin (LSB) facies by the presence of volcanic ash, occurring in distinct layers and disseminated throughout the USB sediments. A thick wedge of interbedded turbidites and hemipelagic sediments fills the Nankai Trough and onlaps the USB in the seaward direction; the outer trench-wedge (OTW) unit defines the distal facies, which is progressively buried by the landward thickening axial trench wedge (ATW). A trench-to-basin transition (TBT) facies is recognized between the USB and OTW units at both sites (Shipboard Scientific Party, 2001a, 2001b).

As expected, the degree of deformation differs between the reference and prism sites. Sediments at Site 1173, well in front of the deformation front, are presumed to have experienced primarily self-weight or normal consolidation during burial. However, minor deformation structures were recognized; for example, discrete, healed normal faults and locally brecciated zones indicate soft-sediment deformation in response to bending of the subducting plate (Shipboard Scientific Party, 2001a). No visible manifestation of the décollement fault was evident at this location; the stratigraphic equivalent of the prism décollement occurs at ~390 meters below seafloor (mbsf) and is defined as the protodécollement horizon (Moore, Taira, Klaus, et al., 2001). A wide range of deformation structures and mesoscopic fabrics were documented at Site 1174, which has been subjected to the initial stages of tectonic deformation (Shipboard Scientific Party, 2001b). Deformation bands were present throughout the shallow trench-wedge units; microfaults and fracture zones were recognized in the deeper TBT, USB, and LSB, commonly associated with incipient thrust faulting. The basal décollement at this site is well developed between 808 and 840 mbsf and characterized by locally intense brecciation, slickenside formation, and mesoscopic fracture foliation (Shipboard Scientific Party, 2001b).

PHYSICAL PROPERTY DATA

Physical property data were collected shipboard for the two drill sites and show distinct variations with lithology, depth, and distance from the deformation front (Shipboard Scientific Party, 2001a, 2001b). Porosity measurements (η) from Site 1173 cores show a general downhole decrease (Fig. **F1**), consistent with normal consolidation with burial (e.g., Athy, 1930; Hamilton, 1976). This decreasing trend, however, is disrupted at ~102 mbsf, where η actually increases from 55%–61% to 62%–68% within ~30 m at the top of the USB (Fig. **F1**). Below this depth, η remains elevated and shows a slight increase to a depth of ~320 mbsf. Between 320 and 344 mbsf at the base of the USB facies, η undergoes a rapid decrease from 62%–66% to 48%–52%. In the deeper LSB facies, porosities appear to resume a more normal decreasing trend with depth, reaching 36%–40% at the base of the hole (Fig. **F1**).

Compressional wave velocity (V_P) is another indicator of sediment state that may vary with porosity, lithology, and cementation. At Site 1173, velocities generally increase with depth, although V_P is essentially constant at ~1600 m/s over an extensive depth range at the top of the

F1. SEM sample locations, η, and V_P, Site 1173, p. 16.

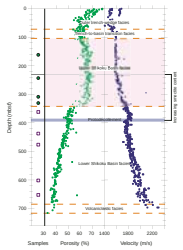

USB, from 83 to 230 mbsf (Fig. F1). Below 230 mbsf, V_P increases gradually to 1800–1840 m/s by 389 mbsf, the protodécollement horizon. Increasing V_P across the USB, despite nearly constant η (Fig. F1), has been interpreted to indicate moderate cementation in these sediments (Shipboard Scientific Party, 2001a). Just below 390 mbsf, V_P shows a slight decrease to 1740–1800 m/s and then resumes the downhole increase, reaching 2200–2300 m/s (Fig. F1).

At Site 1174, both η and V_P show more typical trends with depth than at Site 1173, but several excursions are evident near lithologic boundaries and fault zones, particularly in the shallower section (Fig. F2). Porosities are observed to decrease gradually across the ATW and OTW, reaching 42%–47% at the top of the TBT facies (~430 mbsf). At the base of this range, V_P values are anomalously high at 2150–2250 m/s (Fig. F2). Downsteps in η and V_P across this boundary also coincide with a sudden drop in dissolved SiO_2 (Shipboard Scientific Party, 2001b), similar to that observed at the base of the USB at Site 1173 (Fig. F1). Porosities define a nearly constant range of 35%–42% throughout the TBT and USB to ~661 mbsf, although locally higher values occur (Fig. F2). High η corresponds to high V_P in the USB, for example, at ~520 and ~655 mbsf (Fig. F2). These anomalous zones may also reflect locally higher degrees of cementation (Shipboard Scientific Party, 2001b).

In the LSB facies, trends in η and V_P are smoother but discontinuous across the décollement zone. In the upper LSB, η decreases gradually, reaching 30%–35% just above the décollement (808 mbsf). Below the décollement (840 mbsf), η jumps to 33%–38% then recommences a more typical η-depth trend in the underthrust sediments, albeit shifted to higher values (Fig. F2). V_P increases with depth, with a step down across the décollement zone. Offsets in η and V_P across the décollement are best explained by overpressures in the subducted sediments (e.g., Moore, Taira, Klaus, et al., 2001; Screaton et al., 2002), although differences in stress magnitudes above and below the décollement may also contribute because of the added tectonic loading in the overthrust package (Morgan and Karig, 1995a). In the décollement, porosities are slightly lower than in the overthrust section (Fig. F2). At Site 808, similar low values for η in the décollement were attributed to isotropic porosity collapse because of high pore fluid pressures along the fault (Morgan and Karig, 1995a).

Clearly, both porosities and velocities at Sites 1173 and 1174 show anomalous zones (Figs. F1, F2), but the origin of these anomalies is not immediately apparent. Arrested consolidation resulting from overpressures, as inferred below the décollement zone (Screaton et al., 2002), should result in covariance of η and V_P. Alternatively, V_P may increase relative to η if interparticle cementation enhances sediment stiffness above that predicted for the consolidation stress (e.g., Karig, 1993; Nobes et al., 1992).

To address the nature of physical property anomalies, we plot V_P measured in the vertical direction against η for the few locations where correlative measurements exist (Figs. F3, F4). Both sites show V_P generally increasing for decreasing η, as expected (e.g., Hamilton, 1979; Hyndman et al., 1993). A reference curve that fits the general trends for both data sets despite lithologic differences clarifies where uncorrelated anomalies occur (Figs. F3, F4). Relative to this curve, the USB sediments at Site 1173 (plotted as solid green circles) exhibit unusually high V_P relative to η (Fig. F3); the deviation from the reference curve is greatest in

F2. SEM sample locations, η, and V_P, Site 1174, p. 17.

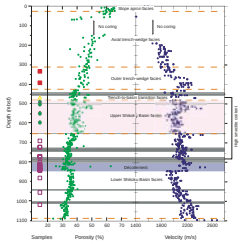

F3. Porosity vs. vertical V_P, Site 1173, p. 18.

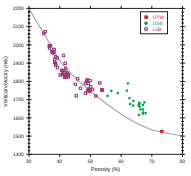

F4. Porosity vs. V_P, Site 1174, p. 19.

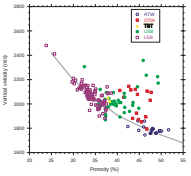

the lower USB. Below this point, the rapid decline in η to 340 mbsf and the subsequent drop in V_P at 390 mbsf recover the original reference curve (Fig. F3). At Site 1174, all data points lie much closer to the reference curve (Fig. F4), although the OTW, TBT, and USB facies do show evidence for high V_P relative to η, consistent with Figure F2. In the LSB strata at both sites, data points fall close to the reference curve despite downhole offsets in V_P and η (Fig. F3, F4), suggesting that high pore pressures are responsible for arrested consolidation in this package (e.g., Screaton et al., 2002).

The anomalies revealed in physical property data for Sites 1173 and 1174 reflect distinct changes in sediment strength and effective stress state, which likely influence where and how deformation initiates and propagates. Previous drill sites along the Nankai margin have also exhibited similar physical property changes; a downhole increase in η was noted at DSDP Site 582, drilled outboard of the prism ~100 km southwest of the Muroto transect (Kagami, Karig, Coulbourn, et al., 1986). The anomalous porosities in the USB have been attributed to high pore fluid pressures (Bray and Karig, 1986, 1988) or to interparticle cementation (e.g., Shipboard Scientific Party, 2001a), both of which impede normal consolidation. Consolidation tests on Site 582 drill cores yielded unusually high shear strengths (Karig, 1993), consistent with a cementation hypothesis (Knipe, 1986; Dadey et al., 1991; Jones, 1994). Additional data in support of the cementation model are now available for Sites 1173 and 1174; the bases of both anomalous η zones coincide with sudden drops in dissolved SiO_2 and lie close to the onset of Cl^- and Na^+ decreases (Shipboard Scientific Party, 2001a, 2001b), all of which are potential indicators of diagenetic changes in the sediments that may modify physical and mechanical properties of the sediments (Schoonmaker, 1986; Tribble and Wilkens, 1994; Kastner et al., 1991; Underwood et al., 1993; **Steurer and Underwood,** this volume). It is probable that the effects of changing physical and pore fluid properties will also be manifested in sediment microstructural and lithologic changes. Here we use SEM analyses of sediments throughout the two drill sites to test these models.

MATERIALS AND METHODS

Samples for SEM analysis were prepared by breaking fragments from recovered cores to obtain a fresh surface. This procedure disturbs the grain orientations at the surface of the fragment much less than cutting does, allowing us to study the preserved microstructures. Samples were then air-dried for at least 24 hr. We also tested the technique of freeze-drying but determined that sample quality was comparable for both methods. Oriented samples were then mounted to expose the bedding plane surfaces and coated with either gold or carbon. The carbon-coated samples had a tendency to charge during SEM analysis; these were then given a thin coating of gold. During SEM analyses, we concentrated on documenting grain size, grain shape, grain arrangement, and degree of dissolution.

Samples for SEM analysis were collected from Site 1173 and 1174 drill cores from a range of facies, seeking representative samples from areas both close to and far from a variety of core-scale deformation structures. Of the nine samples chosen from Site 1173, ranging in depth from 162.4 to 654.5 mbsf, four derive from the USB facies and five are from the LSB facies (Fig. F1). Three of the Site 1173 samples were col-

lected from faulted or fractured intervals. Thirty-five samples from Site 1174 were collected over a depth range from 258.26 to 1017.9 mbsf (Fig. F2). Four samples were collected from the trench-wedge (ATW and OTW) facies, two from the TBT facies, seven from the USB facies, and the remaining twenty-three samples are from the LSB facies. Seventeen of the Site 1174 samples are from locations that show little evidence for discrete deformation. The remaining half of the samples were sampled adjacent to or in core-scale deformation structures.

RESULTS

A wide variety of microstructures and microfabrics can develop as clay-rich sediments accumulate at the seafloor, consolidate during burial, and are subjected to deformation and diagenesis. Using several published descriptions (e.g., Collins and McGown, 1974; van Olphen, 1977; Bennett et al., 1991), we introduce terms to describe the common particle associations and microfabrics we observe in our samples. Clay minerals commonly form aggregates or clusters in the sediment matrix. These originate by particle flocculation during deposition at the seafloor and are preserved during burial (e.g., Bennett et al., 1991); the grain size can be quite large. We recognize two types of aggregates: (1) stacked arrangements of clay platelets and (2) random arrangements of clay particles. Elsewhere, clay minerals are arranged as dispersed individual platelets. An open microstructure or texture is characterized by a range of particle or aggregate sizes and orientations and the presence of abundant pore spaces. Typically, open textured sediments show a low degree of clay mineral preferred orientation (CPO). Domains of parallel or interweaving particles are often separated by regions composed of more randomly oriented particles. With increasing CPO, the planar domains begin to dominate the microstructure, culminating in a penetrative planar fabric.

Site 1173 Sediment Microstructure

Sediments recovered at Site 1173 are thought to have experienced only uniaxial consolidation during burial, providing an opportunity to examine changes in microstructure and microfabric associated with depth and lithology. These studies may also clarify the causes and effects of the observed physical property anomalies. To document first-order changes in sediment microfabric at Site 1173, we initially examined samples derived from locations lacking core-scale deformation structures.

Most of the sediments recovered from the USB exhibit open porous textures, characterized by complex arrangements of random clay aggregates, silt grains, and, less commonly, ash shards and biogenic fragments. This can be observed in examples from the USB. The shallow Sample 190-1173A-18H-3, 25–30 cm (162.39 mbsf), contains large angular pore spaces and relatively coarse particles and aggregates (2–8 µm in diameter, Fig. F5A); deeper examples (e.g., Sample 190-1173A-35X-6, 114–118 cm [330.18 mbsf]) show a wider range of particle sizes and shapes (Fig. F5B). The larger grains consist of stacked or random aggregates, ranging from ~4.7 to ~10.5 µm in diameter. The rough surface texture of this sample reflects the presence of fine clay particles, ranging from ~1.5 to ~3.6 µm in length, which are adhered to aggregate surfaces and dispersed throughout the volume.

F5. Clay microstructural changes, Site 1173, p. 20.

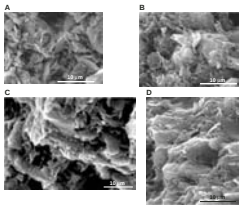

Sediments from the LSB exhibit better developed CPO but also show significant variability. Sample 190-1173A-39X-1, 76–99 cm (360.70 mbsf), near the top of the LSB, contains large stacked clay aggregates that define subhorizontal domains marking the bedding plane (Fig. F5C). The rest of the sample, however, still exhibits a wide mixture of grain sizes, shapes, and orientations, similar to the USB samples (Fig. F5B). At greater depth, specifically below the protodécollement horizon at 390 mbsf, the character and arrangement of the clay particles changes dramatically. As shown by Sample 190-1173A-64X-2, 104–125 cm (602.08 mbsf) (Fig. F5D), dispersed, subparallel but interweaving clay particles define a higher degree of CPO and are commonly oriented subhorizontally. Particle sizes are more uniform, defining a coarse-grained fraction of ~5–10 µm in diameter; particle shapes are regular, and edges of the platelets are relatively smooth.

Sediment microfabrics prove to be much more variable when associated with core-scale deformation structures, although particle sizes and shapes remain similar to those found in the surrounding materials. For example, Sample 190-1173A-33X-4, 117–122 cm, was collected from the USB (308.31 mbsf) adjacent to a zone of small, anastomosing, healed normal faults (Shipboard Scientific Party, 2001a). In this sample, densely packed, stacked aggregates of clay particles define a more developed CPO (Fig. F6A) and a range of particle sizes is still evident. Sample 190-1173A-47X-2, 132–134 cm (439.26 mbsf), derives from a region of foliated breccia in the LSB, characterized by discrete fragments with polished surfaces (Shipboard Scientific Party, 2001a). The microstructure of this sample is open but shows relatively close packing of large and small clay particles and aggregates and a poorly developed subhorizontal CPO (Fig. F6B). Clay alignment is extreme, and particles cannot be distinguished on slickensided slip surfaces (Fig. F6C). Sample 190-1173A-69X-5, 78–85 cm (654.52 mbsf), was collected close to a healed normal fault in the LSB (Shipboard Scientific Party, 2001a). The fabric is similar to other samples from this area, showing discrete interweaving clay particles with uniform grain size and shape and moderately developed CPO (Fig. F6D).

F6. Microstructural changes associated with core-scale structures, Site 1173, p. 21.

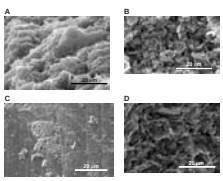

Site 1174 Sediment Microstructures

Sediments at Site 1174 are expected to have experienced both vertical consolidation during burial and tectonic deformation accompanying accretion. The associated microstructures and clay fabrics may be highly variable as a result. We highlight downhole changes in the development and orientation of CPO, as well as in grain size and shape, as indicated by SEM images. These can be compared to regions with and without core-scale deformation features and to samples from Site 1173.

Samples collected from the trench-wedge units (ATW and OTW) and USB show a very heterogeneous fabric. OTW Sample 190-1174B-21R-2, 46–49 cm (335.06 mbsf), is representative and exhibits large stacked aggregates of particles, separated by domains containing smaller, more random aggregates and fine dispersed grains; the surfaces of the aggregates are very rough (Fig. F7A). The CPO is subhorizontal and parallel to bedding. Similar open textures define the USB samples as well. Sample 190-1174B-37R-5, 64–68 cm (492.34 mbsf), consists of very irregularly shaped particles and aggregates with a range of sizes (Fig. F7B). In this view, they show a poorly developed, inclined CPO. Denser particle packing and further alignment of clay particles are evident deeper in the USB (e.g., Sample 190-1174B-43R-5, 128–150 cm [550.88 mbsf],

F7. Microstructural changes, Site 1174, p. 22.

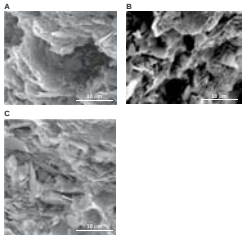

shown in Figure F7C). The CPO in this sample is more developed than above and defined by thicker, closely spaced, stacked arrangements of clay minerals. Orientation of CPO in this view is ~33° from the horizontal. These samples contrast with those observed at Site 1173 by their denser packing and better developed CPO, but both examples show similar particle sizes, shapes, and roughness.

Sediments in the LSB at Site 1174 resemble those of Site 1173 in the same unit. Particles are dispersed but are generally aligned; particle shapes and sizes are more uniform, and edges are smooth. Samples 190-1174B-58R-3, 11–15 cm (691.11 mbsf), and 69R-7, 4–7 cm (801.41 mbsf), show relatively dense packing of clay minerals, although small pore spaces are quite abundant (Fig. F8A, F8B). Particle sizes range from ~3 to ~8 µm. The finer, dispersed clay phase noted upsection (e.g., Fig. F7) is absent in these and deeper samples. Samples in the LSB, both above and below the décollement zone (e.g., Sample 190-1174B-85R-6, 64–69 cm [955.24 mbsf]) also exhibit a well-developed CPO, defined by the alignment of discrete interweaving clay platelets (Fig. F8C). In these samples, pore spaces are distinctly flattened and elongated.

More complicated microstructures and fabrics are present in the vicinity of discrete deformation structures in the drill cores. Sample 190-1174B-13R-2, 56–58 cm (258.26 mbsf), was collected adjacent to deformation bands from the ATW facies (Shipboard Scientific Party, 2001b). Shown at two scales in Figure F9, this sample displays two intersecting fabric planes: a penetrative bedding-parallel CPO defined by stacked aggregates of clay particles crosscut by oblique, spaced fabric planes oriented ~24° from the horizontal. The grain size and shape distributions resemble those of other samples in the shallow section (e.g., Fig. F7).

Samples 190-1174B-35R-1, 52–53 cm (467.62 mbsf), and 35R-2, 84–87 cm (469.44 mbsf), were collected from fractured intervals in the TBT, identified as part of the incipient thrust (Shipboard Scientific Party, 2001b). In contrast to samples from similar depths away from such deformation structures (e.g., Fig. F7), these sediments exhibit a highly developed CPO through oriented stacked aggregates (Fig. F10A) and locally intense clay realignments along slickensided surfaces (Fig. F10B); CPO intensity was observed to decrease with distance from the slip surfaces. Sample 190-1174B-38R-6, 119–124 cm (503.99 mbsf), comes from a fracture zone in the USB (Shipboard Scientific Party, 2001b) and also shows enhanced CPO. Again, two intersecting fabric planes are evident: a subhorizontal plane defined by small stacked assemblages of particles and an oblique crosscutting fabric, subparallel to the slip surfaces (Fig. F11). This arrangement defines an incipient scaly, or S-C, fabric (e.g., Moore et al., 1986; Snoke et al., 1998). In this particular sample, the smaller, dispersed clay phase, noted elsewhere in the USB samples, is less evident; the rough texture of the stacked aggregates suggests that these fine particles may have been entrained and reoriented parallel to the inclined fabric (Fig. F11B).

The LSB contains numerous faults and fracture zones, including the décollement zone, and many samples reveal deformation-induced microfabric. Sample 190-1174B-66R-5, 32–36 cm (770.92 mbsf), derives from a zone of inclined intersecting fractures (Shipboard Scientific Party, 2001b), and polished surfaces of the clay fragments reflect slip planes. The CPO is intense and penetrative close to the slip planes, and the fabric plane is oriented at a very high angle to the bedding (Fig. F12A). Samples collected from in the décollement zone (~808–840 mbsf) exhibit moderate to well-developed CPO. Generally, CPO intensity increases with depth, consistent with the intensification of fractur-

F8. Microstructural characteristics in the LSB, Site 1174, p. 23.

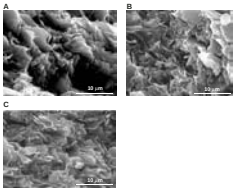

F9. Intersecting fabric planes, p. 24.

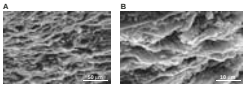

F10. Samples from the incipient thrust zone, Site 1174, p. 25.

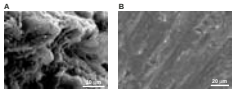

F11. Incipient scaly fabric associated with fracture zones, p. 26.

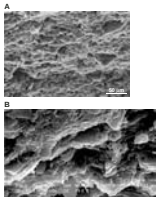

F12. Samples from deformed LSB sediments, Site 1174, p. 27.

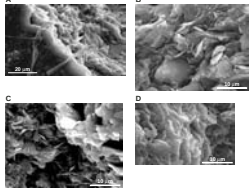

ing and brecciation (Shipboard Scientific Party, 2001b). Sediments near the top of the décollement (e.g., Samples 190-1174B-71R-2, 69–73 cm [813.57 mbsf], and 71R-3, 23–28 cm [814.39 mbsf]) display subparallel packing of discrete particles of uniform size and shape (Fig. **F12B, F12C**). Deeper in the décollement zone, Sample 190-1174B-73R-5, 53–55 cm (838.33 mbsf), reveals a more intense CPO, defined by alignment and stacking of closely packed particles (Fig. **F12C**). Again, in these LSB sediments, the smaller particle phase observed in the shallower sediments is lacking.

DISCUSSION

Our SEM analyses of sediment microstructures from Sites 1173 and 1174 reveal systematic changes in clay mineral fabric, arrangement, grain shape and size. These changes prove to correlate well with variations in key physical properties, lithology, and deformation structures. Additional data relating to pore water chemistry, mineralogy, and grain size provide further insight into the origin of these variations and their implications for prism structure and evolution.

A porous open microstructure, composed of a wide size range of irregularly shaped, randomly oriented particles, characterizes sediments in the shallower units (i.e., ATW, OTW, TBT, and USB). This holds true at both sites but is most evident at Site 1173, as the anomalously high porosities in the USB has preserved the microstructure (Fig. **F5A, F5B**). Downhole, we see the increasing development of CPO—the primary control is burial depth and compaction that leads to enhanced clay mineral alignment parallel to the bedding plane. At Site 1174, however, sediments show a greater tendency to develop inclined fabrics, particularly adjacent to deformation bands and fracture zones (Figs. **F9, F10, F11**). LSB samples generally show enhanced CPO, generally parallel to bedding at Site 1173 (Fig. **F5C, F5D**) and often inclined at Site 1174 (Fig. **F8**). At intermediate depths, where CPO becomes apparent in the SEM images (e.g., Figs. **F5C, F7**), the fabric is often defined by stacked aggregates or domains of aligned particles, separated by regions of more randomly oriented grains. This domainal structure becomes less apparent as the clay alignment becomes better developed with depth.

A distinct change in sediment texture takes place with depth and is most noticeable by comparison of USB and LSB sediments. In the USB samples at Site 1173, the sediment matrix is very heterogeneous, with a wide range of grain sizes, shapes, and arrangements. In addition, we recognize a distinctive fine-grained clay phase disseminated throughout the matrix, imparting a rough surface texture to the grains (e.g., Fig. **F5B, F5C**). **Steurer and Underwood** (this volume) show a downward increase in the weight percentage of smectite across these zones, providing a plausible identification for the fine-grained phase. In contrast, our deeper LSB samples are more homogeneous; dispersed but aligned clay particles are smoother and more uniform in shape, size, and fabric (Figs. **F5D, F8, F12**). Mineralogic data indicate lower smectite abundance in these samples and increased illite (**Steurer and Underwood,** this volume).

The presence of a fine smectite clay phase in the USB high-porosity zone at Site 1173 suggests that it might serve as a cementing agent; the role of clays in supporting the sediment matrix was also hypothesized by **Ujiie et al.** (this volume). The decrease in porosity at the base of the USB (Fig. **F1**) may reflect the onset of smectite to illite diagenesis, lead-

ing to breakdown of the cementing phase. Pore water chemistry shows marked decreases in both Cl^- and Na^+ below this boundary, consistent with downhole freshening of the pore fluids by smectite dehydration reactions (e.g., **Steurer and Underwood,** this volume) or influx of low-salinity fluids from deeper within the prism (Kastner et al., 1991, 1993; Spivack et al., 2002). The fine-grained phase correlated with smectite, however, is also observed in the upper LSB at Site 1173 (Fig. **F5C**) and in shallow lithologic units at Site 1174 (Figs. **F7, F10**), again consistent with the mineralogic data (**Steurer and Underwood,** this volume). The distribution and character of this phase does not change noticeably among these facies. This argues that the fine-grained phase does not support the matrix of the USB sediments against porosity collapse by itself.

A better correlation with relative smectite abundance may be provided by V_P, which increases smoothly downhole to the protodécollement at Site 1173; no deflection is evident across the transition in η at the USB/LSB boundary (Fig. **F1**). Both the weight percentage of smectite and V_P drop below this horizon (**Steurer and Underwood,** this volume; Shipboard Scientific Party, 2001a). Furthermore, at the resolution of our samples, the protodécollement marks the downhole transition in sediment textures in our SEM samples and the homogenization of clays and clay fabric, likely reflecting greater illite content. Smectite, for example, grown authigenically at grain boundaries, may serve to increase sediment stiffness in the sediments above the protodécollement (e.g., Dadey et al., 1991). The presence of disseminated clay particles in the matrix can lead to greater sediment coupling, increasing V_P relative to units with lower smectite abundance, even if the clay is not a primary cementing agent in the USB.

The protodécollement horizon at Site 1173, therefore, appears to separate two domains, distinguished by mineralogy, physical properties, and clay microstructure. The documented decrease in smectite abundance at the protodécollement and associated change in microstructure point to a diagenetically controlled boundary corresponding to the smectite to illite transition (e.g., **Steurer and Underwood,** this volume). Enhanced temperature and pressures cause the progressive illitization of the clay particles and the release of smectite interlayer water (Kastner et al., 1991). The resulting freshening of the deeper pore waters and high vertical stresses may favor the growth of dispersed but well-aligned illite particles (e.g., van Olphen, 1977; Mitchell, 1993), producing the distinct sediment textures that we see in the lower LSB.

If the anomalous zone of porosity at Site 1173 cannot be explained by a cementing phase of smectite, alternatively it may result from precipitation of opal-A, derived from dissolution of biogenic silica and ash (e.g., Kastner, 1981; Nobes et al., 1992; Shipboard Scientific Party, 2001a). The sharp drop in dissolved silica at the Site 1173 USB/LSB boundary has been tentatively correlated with the position of the opal-A to opal-CT transition, although the sediments do not contain high biogenic silica (Shipboard Scientific Party, 2001a). Similar porosity steps have been documented at other ODP sites (e.g., in the Japan Sea) and may reflect the dissolution of cementing contacts, allowing porosity collapse (e.g., Nobes et al., 1992); additionally, the presence of opal CT is commonly correlated with increased velocities, which is consistent with the smooth increase in V_P across the USB/LSB boundary.

The projection of the primary lithologic and diagenetic characteristics noted at Site 1173 into the prism at Site 1174 is complicated by the

tectonic overprint in the PTZ. As at Site 1173, the relative weight percentage of smectite generally increases downhole throughout the USB and upper LSB but begins to decline at ~740 mbsf, well above the décollement horizon (**Steurer and Underwood,** this volume). From the SEM images, we also note that sediment microstructure begins to homogenize at a higher stratigraphic level at Site 1174 than at Site 1173 (by ~690 mbsf) (Fig. **F8A**), although textures remain variable down to at least ~770 mbsf (e.g., Fig. **F12A**). Higher pressure and temperature conditions in the PTZ result in further progression of the smectite to illite transformation relative to the reference site (**Steurer and Underwood,** this volume).

Site 1174 pore fluid chemistry data also exhibit a drop in SiO_2, similar to the one recognized at the USB/LSB boundary at Site 1173. In the PTZ, however, this drop lies at the base of the OTW and corresponds to small steps down in porosity and V_P (Fig. **F2**). Slightly enhanced V_P above this boundary may relate to higher opal-CT content (Shipboard Scientific Party, 2001b). The lower excursion in porosities in the OTW at Site 1174, relative to that in the USB at Site 1173, may be a result of tectonically induced lateral shortening in this unit. Increased lateral stresses sufficient to overcome the enhanced matrix strength would lead to partial porosity collapse and densification. This may also explain the higher degree and greater obliquity of CPO in samples from the OTW (e.g., Fig. **F7A**). Similarly, sediment fabrics associated with deformation bands in both the ATW and OTW show well-developed intersecting fabric planes consistent with distributed tectonic shortening of the sediment matrix (Fig. **F9**).

Furthermore, throughout Site 1174, sediment CPOs are more intense and tend toward greater inclinations from the horizontal than noted at Site 1173, particularly in the shallower USB, TBT, and trench-wedge units (Figs. **F7, F9**). This pattern is consistent with tectonic shortening in the PTZ, leading to distributed deformation and bulk realignment of the sediment matrix, as well as formation of discrete deformation structures (Karig and Lundberg, 1990; Morgan and Karig, 1995b). In association with deformation structures, including the décollement zone, CPO intensity tends to increase, although it continues to be highly variable. This suggests the influence of locally high shear stresses coupled with pore fluid fluctuations and sediment heterogeneity.

The coincidence of the protodécollement horizon and the transitions in smectite abundance and sediment microfabric at Site 1173 identify several potential controls on the position of this critical structural boundary. The slight drop in V_P at this horizon indicates a strength contrast that may tend to localize slip in the deeper, lower-strength materials (e.g., Moore, Taira, Klaus, et al., 2001). Furthermore, the character of the microfabrics in the deeper LSB may favor sliding—the spaced, planar fabric subparallel to bedding and uniform sizes and shapes of the clay minerals define favorable slip planes (e.g., Yan et al., 2001). Our microstructural evidence suggests that these characteristics are absent in the overlying strata. These results provide important new evidence for preferential localization of the Nankai décollement during the very early stages of accretion.

CONCLUSIONS

Our analysis of SEM microstructural data for sediments from the Nankai Trough and frontal prism provides valuable insight into the

fundamental changes in clay fabrics with depth, lithology, and deformation. Our key observations and interpretations include the following:

1. The increasing consolidation of sediments with burial is recorded by increasing development of bedding-parallel CPO, although this progress is retarded throughout the high-porosity USB facies at Site 1173.
2. Clay microstructures are similar both in and below the anomalous porosity zone at Site 1173, providing little evidence for a cementing clay phase. Progressive downhole increase in compressional velocity (V_P) across the porosity jump is more consistent with a transition from opal-A to opal-CT, suggesting that minor amounts of silica serve as the cementing material in the USB.
3. The matrix of sediments collected close to discrete core-scale deformation structures, ranging from pretectonic microfaults in the Shikoku Basin to tectonically induced deformation bands, fractures, faults, and the décollement zone, generally exhibits more intense CPO and a tendency toward greater inclination of the fabric planes. This strongly suggests that tectonic loading induces bulk deformation of the sediment, leading to particle rotation and realignment.
4. Distinct downhole changes in microstructure are observed at both sites and appear to correlate with lithology, mineralogy, and physical properties. Shallow sediments exhibit very heterogeneous, open textures, defined by the presence of coarse clay aggregates and disseminated fine clay particles. Deeper sediments show increased homogenization of grain size and shape, loss of clay aggregates, coarsening of the clay phase, and development of subhorizontal CPO. This transition correlates with the downhole decrease in the weight percentage of smectite at both sites and with a slight step down in V_P at reference Site 1173, which is interpreted to result from progressive illitization of clays with increasing pressure and temperature. This transition coincides with the depth of the protodécollement horizon at the reference Site 1173, yet lies above the correlative décollement zone at Site 1174 in the PTZ.
5. The contrasting physical properties and clay microfabrics on either side of the protodécollement at Site 1173 may favor localization of bedding-parallel slip as the décollement propagates seaward, suggesting that the location of this primary fault plane may be defined very early during the accretion process.

ACKNOWLEDGMENTS

This research used samples and data provided by the Ocean Drilling Program (ODP). ODP is sponsored by the U.S. National Science Foundation (NSF) and participating countries under management of Joint Oceanographic Institutions (JOI), Inc. Funding for this research and partial graduate stipend for E. Blanche Sunderland was provided by JOI grant number F001240. We also thank Kitty L. Milliken (University of Texas at Austin, Department of Geological Sciences) and Scott Stookey (CoreLab, Houston, Texas) for providing valuable assistance and advice on SEM analysis and interpretation. In addition, we thank Mike B.

Underwood for providing advance copies of lithology and grain size data for comparison with our results. Kevin M. Brown and one anonymous reviewer provided very helpful comments that inspired a careful reconsideration of our interpretations, leading to a much improved manuscript.

REFERENCES

Athy, L.F., 1930. Density, porosity, and compaction of sedimentary rocks. *AAPG Bull.,* 14:1–24.

Bennett, R.H., O'Brien, N.R., and Hulbert, M.H., 1991. Determinants of clay and shale microfabric signatures: processes and mechanisms. *In* Bennett, R.H., Bryant, W.R., and Hulbert, M.H. (Eds.), *Microstructure of Fine-Grained Sediments: From Mud to Shale:* New York (Springer-Verlag), 5–32.

Bray, C.J., and Karig, D.E., 1985. Porosity of sediments in accretionary prisms and some implications for dewatering processes. *J. Geophys. Res.,* 90:768–778.

————, 1986. Physical properties of sediments from the Nankai Trough, Deep Sea Drilling Project Leg 87A, Sites 582 and 583. *In* Kagami, H., Karig, D.E., Coulbourn, W.T., et al., *Init. Repts. DSDP,* 87: Washington (U.S. Govt. Printing Office), 827–842.

————, 1988. Dewatering and extensional deformation of the Shikoku Basin hemipelagic sediments in the Nankai Trough. *Pure Appl. Geophys.,* 128:725–747.

Collins, K., and McGown, A., 1974. The form and function of microfabric features in a variety of natural soils. *Geotechnique,* 24:223–254.

Dadey, K.A., Leinen, M., and Silva, A.J., 1991. Anomalous stress history of sediments of the northwest Pacific: the role of microstructure. *In* Bennett, R.H., Bryant, W.R., and Hulbert, M.H. (Eds.), *Microstructure of Fine-Grained Sediments: From Mud to Shale:* New York (Springer-Verlag), 229–236.

Hamilton, E.L., 1976. Variations of density and porosity with depth in deep-sea sediments. *J. Sediment. Petrol.,* 46:280–300.

————, 1979. Sound velocity gradients in marine sediments. *J. Acoust. Soc. Am.,* 64:909–922.

Hyndman, R.D., Moore, G.F., and Moran, K., 1993. Velocity, porosity, and pore-fluid loss from the Nankai subduction zone accretionary prism. *In* Hill, I.A., Taira, A., Firth, J.V., et al., *Proc. ODP, Sci. Results,* 131: College Station, TX (Ocean Drilling Program), 211–220.

Jones, M., 1994. Mechanical principles of sediment deformation. *In* Maltman, A. (Ed.), *The Geological Deformation of Sediments:* London (Chapman and Hall), 37–71.

Kagami, H., Karig, D.E., Coulbourn, W.T., et al., 1986. *Init. Repts. DSDP,* 87: Washington (U.S. Govt. Printing Office).

Karig, D.E., 1993. Reconsolidation tests and sonic velocity measurements of clay-rich sediments from the Nankai Trough. *In* Hill, I.A., Taira, A., Firth, J.V., et al., *Proc. ODP, Sci. Results,* 131: College Station, TX (Ocean Drilling Program), 247–260.

Karig, D.E., and Angevine, C.L., 1986. Geologic constraints on subduction rates in the Nankai Trough. *In* Kagami, H., Karig, D.E., Coulbourn, W.C., et al., *Init. Repts. DSDP,* 87: Washington (U.S. Govt. Printing Office), 789–796.

Karig, D.E., and Lundberg, N., 1990. Deformation bands from the toe of the Nankai accretionary prism. *J. Geophys. Res.,* 95:9099–9109.

Kastner, M., 1981. Authigenic silicates in deep sea sediments: formation and diagenesis. *In* Emiliani, C. (Ed.), *The Sea* (Vol. 7): *The Oceanic Lithosphere:* New York (Wiley), 915–980.

Kastner, M., Elderfield, H., Jenkins, W.J., Gieskes, J.M., and Gamo, T., 1993. Geochemical and isotopic evidence for fluid flow in the western Nankai subduction zone, Japan. *In* Hill, I.A., Taira, A., Firth, J.V., et al., *Proc. ODP, Sci. Results,* 131: College Station, TX (Ocean Drilling Program), 397–413.

Kastner, M., Elderfield, H., and Martin, J.B., 1991. Fluids in convergent margins: what do we know about their composition, origin, role in diagenesis and importance for oceanic chemical fluxes? *Philos. Trans. R. Soc. London A,* 335:243–259.

Knipe, R.J., 1986. Faulting mechanisms in slope sediments: examples from Deep Sea Drilling Project cores. *In* Moore, J.C. (Ed.), *Structural Fabric in Deep Sea Drilling Project Cores from Forearcs.* Mem.—Geol. Soc. Am., 166:45–54.

Mitchell, J.K., 1993. *Fundamentals of Soil Behavior* (2nd ed.): New York (Wiley).

Moore, G.F., Taira, A., Klaus, A., et al., 2001. *Proc. ODP, Init. Repts.,* 190 [CD-ROM]. Available from: Ocean Drilling Program, Texas A&M University, College Station TX 77845-9547, USA.

Moore, G.F., Taira, A., Klaus, A., and Leg 190 Scientific Party, 2001. New insights into deformation and fluid flow processes in the Nankai Trough accretionary prism: results of Ocean Drilling Program Leg 190. *Geochem. Geophys. Geosyst.,* 2:10.129/2001GC000166.

Moore, J.C., Roeske, S.M., Lundberg, N., Schoonmaker, J., Cowan, D.S., Gonzales, E., and Lucas, S.E., 1986. Scaly fabrics from Deep Sea Drilling Project cores from forearcs. *In* Moore, J.C. (Ed.), *Structural Fabric in Deep Sea Drilling Project Cores from Forearcs*. Mem.—Geol. Soc. Am., 166:55–73.

Morgan, J.K., and Karig, D.E., 1995a. Décollement processes at the Nankai accretionary margin, Southeast Japan. *J. Geophys. Res.,* 100:15221–15231.

————, 1995b. Kinematics and a balanced and restored cross-section across the toe of the eastern Nankai accretionary prism. *J. Struct. Geol.,* 17:31–45.

Nobes, D.C., Murray, R.W., Kuramoto, S., Pisciotto, K.A., and Holler, P., 1992. Impact of silica diagenesis on physical property variations. *In* Pisciotto, K.A., Ingle, J.C., Jr., von Breymann, M.T., Barron, J., et al., *Proc. ODP, Sci. Results,* 127/128 (Pt. 1): College Station, TX (Ocean Drilling Program), 3–31.

Schoonmaker, J., 1986. Clay mineralogy and diagenesis of sediments from deformation zones in the Barbados accretionary wedge (DSDP Leg 78A). *In* Moore, J.C. (Ed.), *Structural Fabric in Deep Sea Drilling Project Cores from Forearcs*. Mem.—Geol. Soc. Am., 166:105–116.

Screaton, E., Saffer, D., Henry, P., Hunze, S., et al., 2002. Porosity loss within the underthrust sediments of the Nankai accretionary complex: implications for overpressures. *Geology,* 30:19–22.

Seno, T., Stein, S., and Gripp, A.E., 1993. A model for the motion of the Philippine Sea plate consistent with NUVEL-1 and geological data. *J. Geophys. Res.,* 98:17941–17948.

Shipboard Scientific Party, 1991. Site 808. *In* Taira, A., Hill, I., Firth, J.V., et al., *Proc. ODP, Init. Repts.,* 131: College Station, TX (Ocean Drilling Program), 71–269.

————, 2001a. Site 1173. *In* Moore, G.F., Taira, A., Klaus, A., et al., *Proc. ODP, Init. Repts.,* 190, 1–147 [CD-ROM]. Available from: Ocean Drilling Program, Texas A&M University, College Station TX 77845-9547, USA.

————, 2001b. Site 1174. *In* Moore, G., Taira, A., Klaus, A., et al., *Proc. ODP, Init. Repts.,* 190, 1–149 [CD-ROM]. Available from: Ocean Drilling Program, Texas A&M University, College Station TX 77845-9547, USA.

Snoke, A.W., Tullis, J., and Todd, V.R. (Eds.), 1998. *Fault Related Rocks: A Photographic Atlas:* Princeton, NJ (Princeton University Press).

Spivack, A.J., Kastner, M., and Ransom, B., 2002. Elemental and isotopic chloride geochemistry and fluid flow in the Nankai Trough. *Geophys. Res. Lett.,* 29:10.1029/2001Glo14122.

Tribble, J.S., and Wilkens, R.H., 1994. Microfabric of altered ash layers, ODP Leg 131, Nankai Trough. *Clays Clay Miner.,* 42:428–436.

Underwood, M.B., Pickering, K., Gieskes, J.M., Kastner, M., and Orr, R., 1993. Sediment geochemistry, clay mineralogy, and diagenesis: a synthesis of data from Leg 131, Nankai Trough. *In* Hill, I.A., Taira, A., Firth, J.V., et al., *Proc. ODP, Sci. Results,* 131: College Station, TX (Ocean Drilling Program), 343–363.

van Olphen, H., 1977. *An Introduction to Clay Colloid Chemistry:* New York (Wiley-Interscience Publ.).

Yan, Y., van der Pluijm, B.A., and Peacor, D.R., 2001. Deformation microfabrics of clay gouge, Lewis Thrust, Canada: a case for fault weakening from clay transformation. *Geol. Soc. Spec. Publ.,* 186:103–112.

Figure F1. Plot of SEM sample locations, porosity, and compressional wave velocity vs. depth for Site 1173. Lithologic boundaries are marked with orange dashed lines, and the USB is highlighted in pink. The proto-décollement is highlighted in blue.

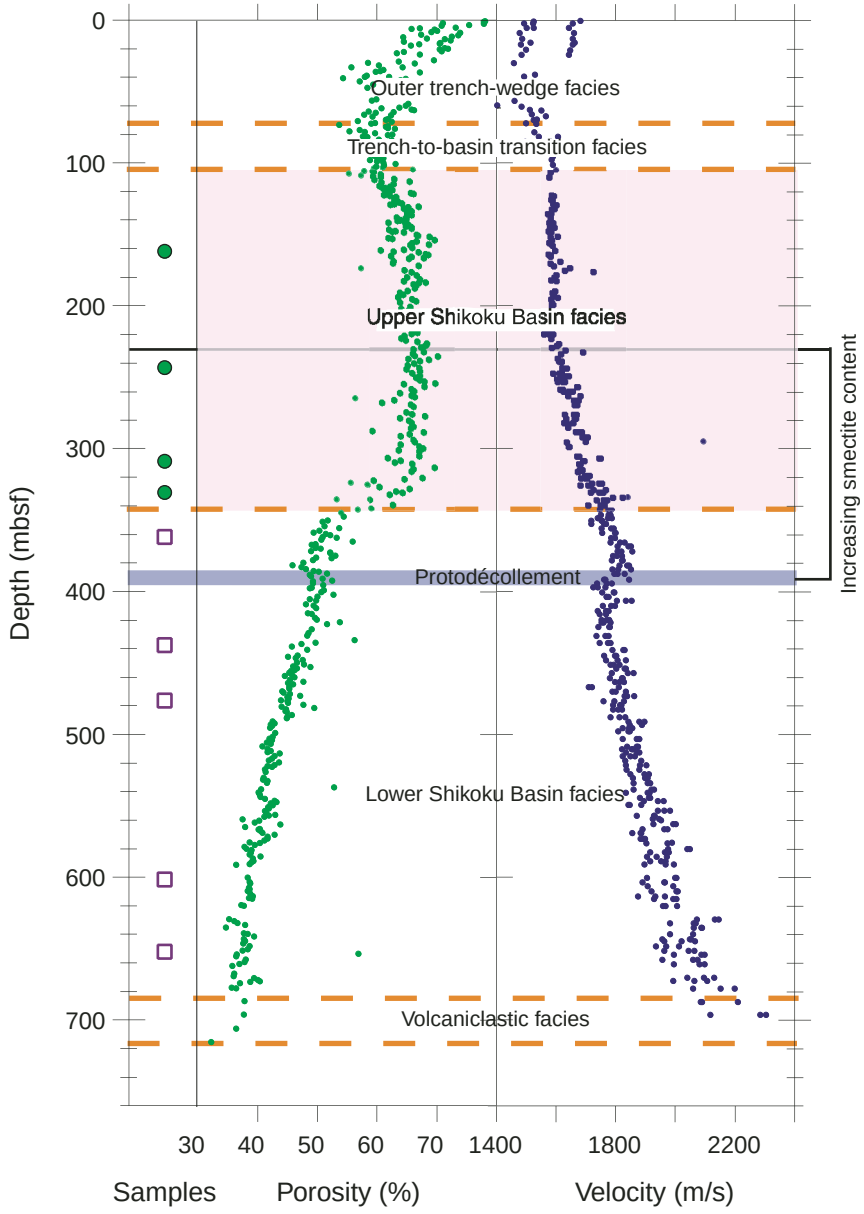

Figure F2. Plot of SEM sample locations, porosity, and compressional wave velocity vs. depth for Site 1174. Lithologic boundaries are marked with orange dashed lines, and the USB is highlighted in pink. The décollement is highlighted in blue, and other fault zones are displayed in shades of gray.

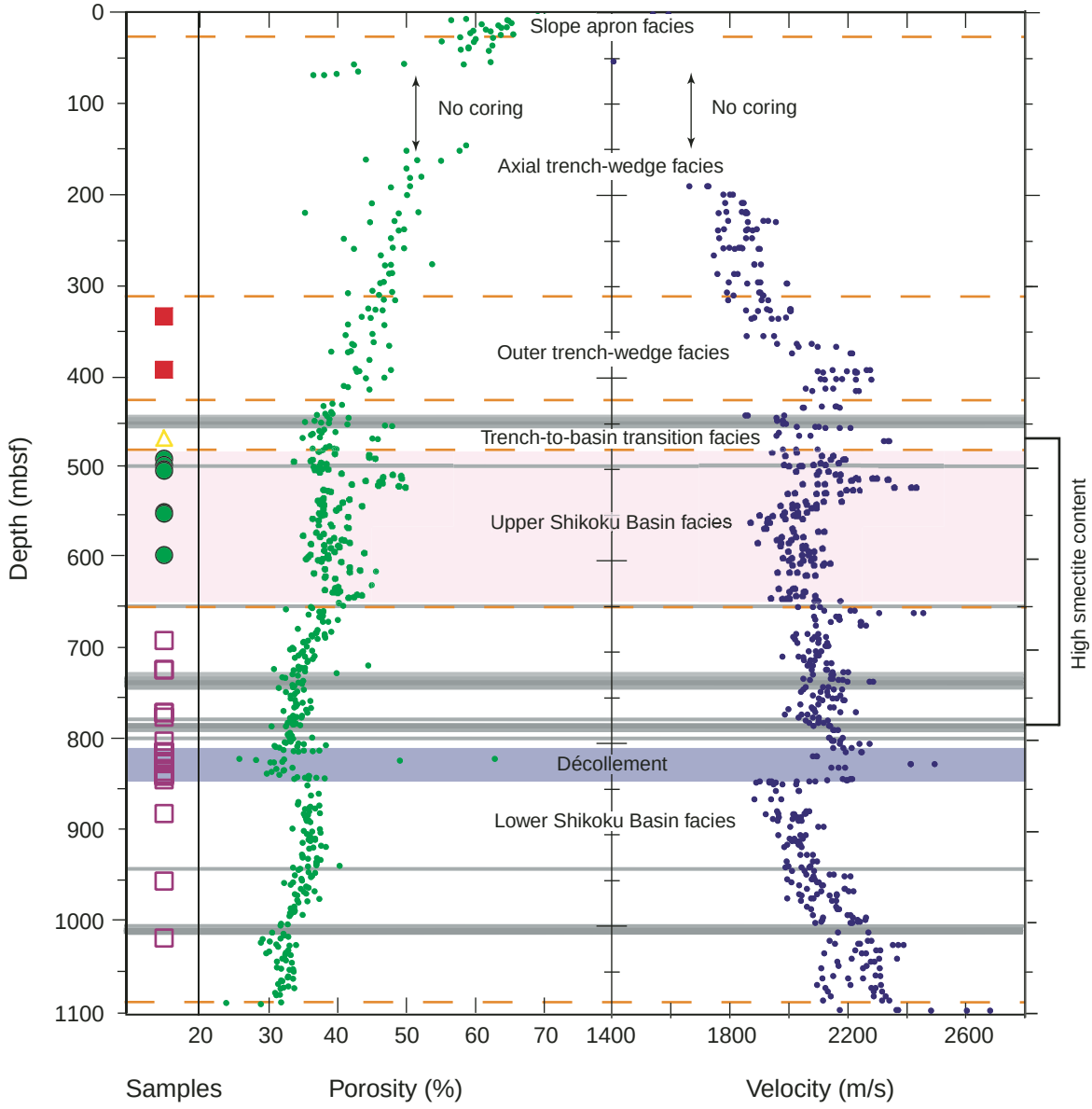

Figure F3. Plot of porosity vs. vertical compressional wave velocity for Site 1173. The gray solid line shows reference curve fit to data from both sites. OTW = outer trench wedge, USB = upper Shikoku Basin, LSB = lower Shikoku Basin.

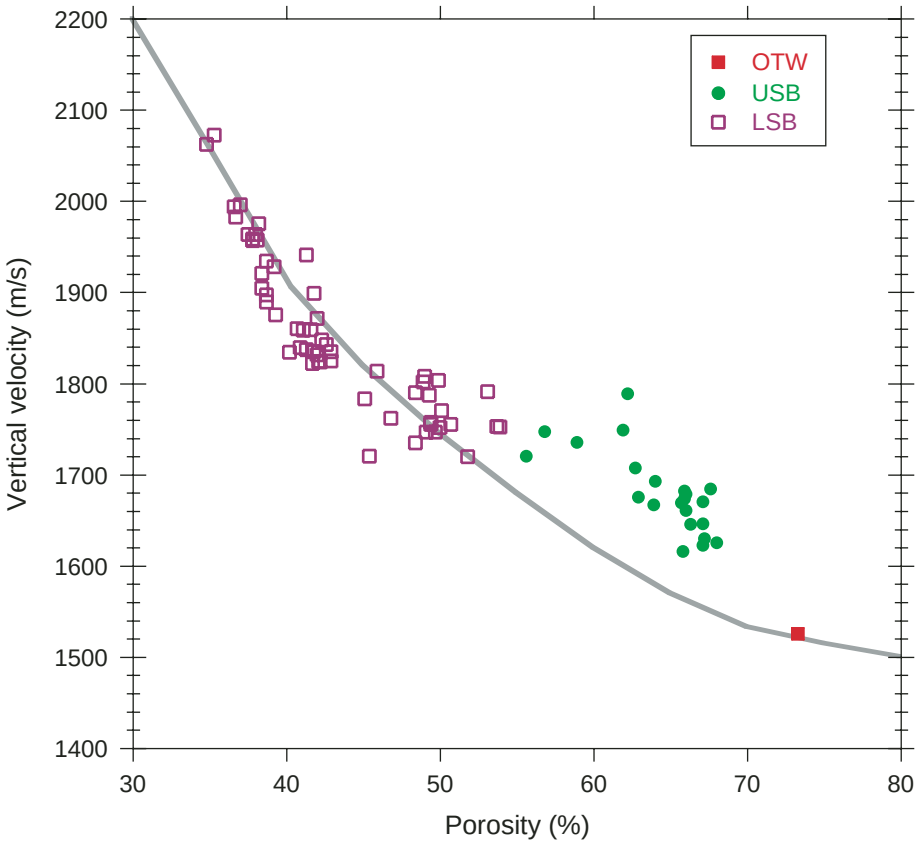

Figure F4. Plot of porosity vs. vertical compressional wave velocity for Site 1174. Gray solid line shows reference curve fit to data from both sites. ATW = axial trench wedge, OTW = outer trench wedge, TBT = trench-to-basin transition, USB = upper Shikoku Basin, LSB = lower Shikoku Basin.

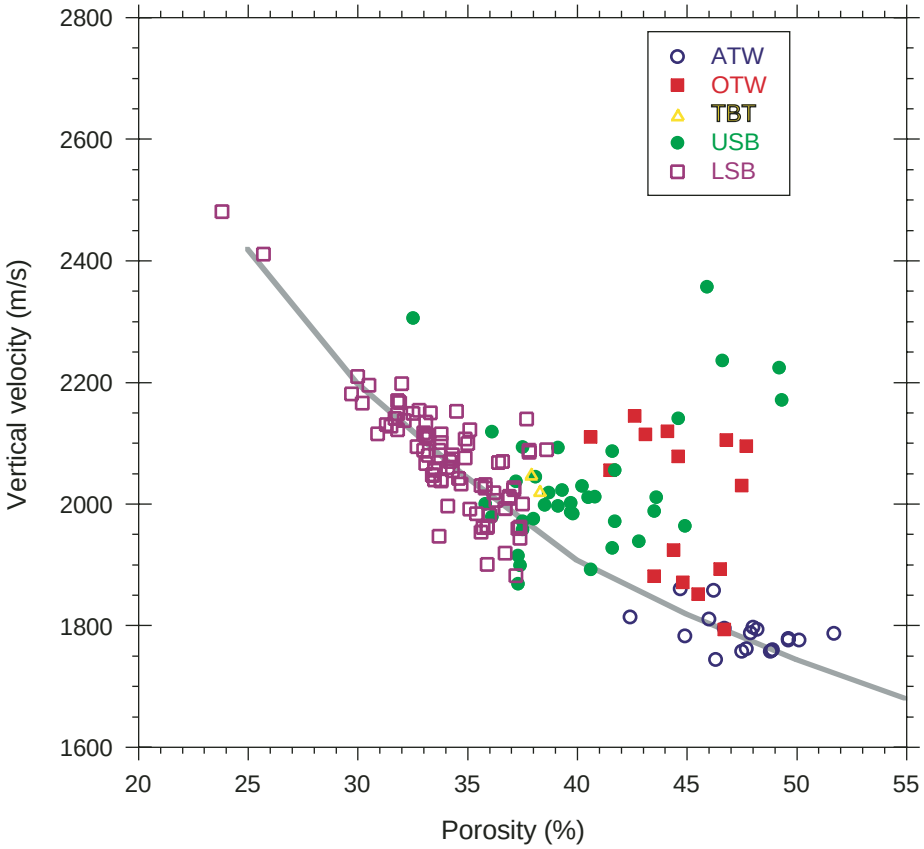

Figure F5. SEM photomicrographs showing clay microstructural changes with depth at Site 1173. The up direction is toward the top of the page. **A.** Open microstructure of USB Sample 190-1173A-18H-3, 25–30 cm. **B.** USB Sample 190-1173A-35X-6, 114–118 cm. Note the presence of both coarse and fine particle sizes. **C.** LSB Sample 190-1173A-39X-1, 76–99 cm, consists of stacked aggregates, separated by more randomly oriented particles. **D.** Dispersed, uniform clay particles showing penetrative CPO of LSB Sample 190-1173A-64X-2, 104–125 cm.

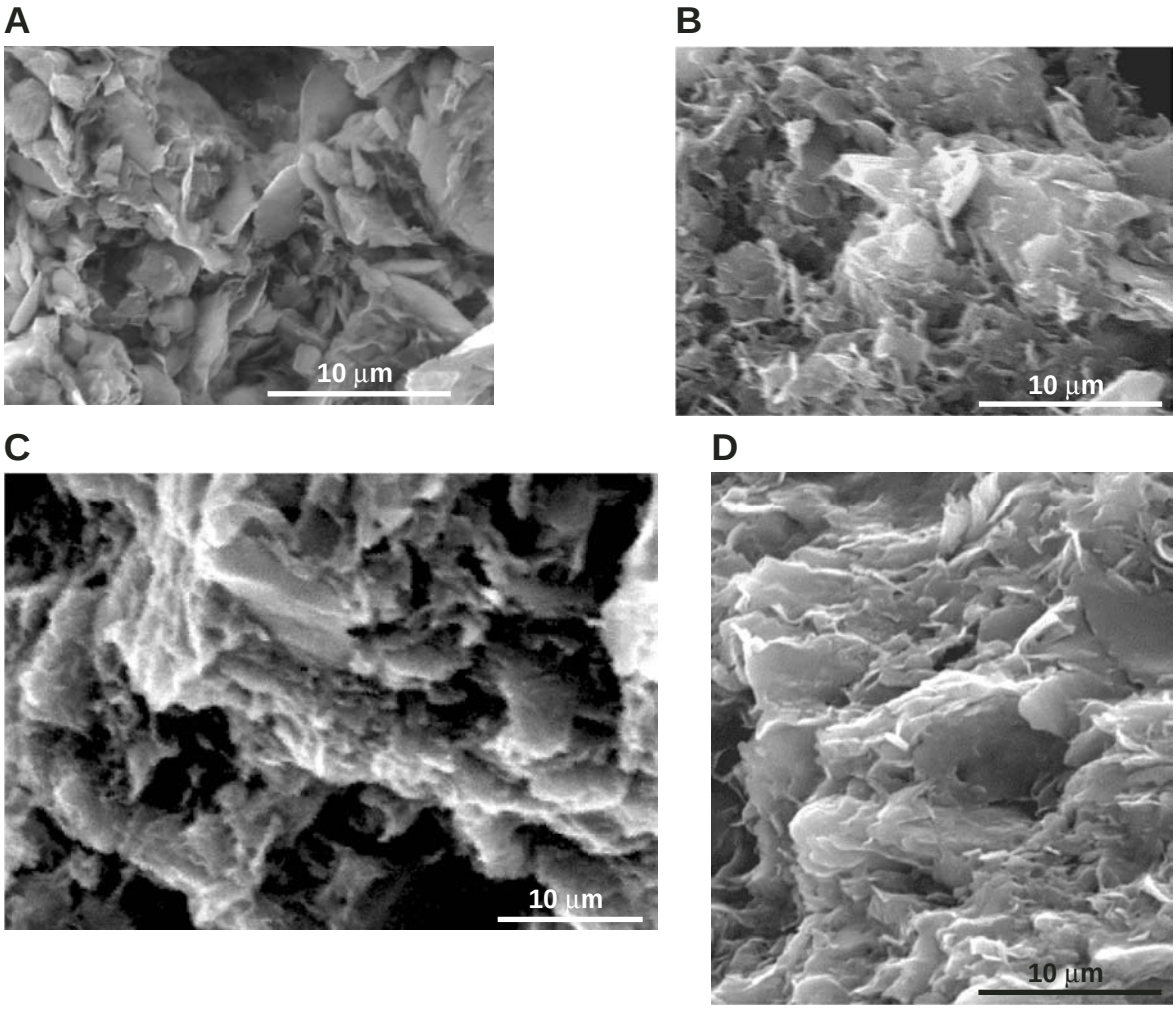

Figure F6. SEM photomicrographs showing microstructural changes associated with core-scale structures at Site 1173. The up direction is toward the top of the page. **A.** USB Sample 190-1173A-33X-4, 117–122 cm, collected adjacent to a healed microfault, exhibits an inclined CPO. **B, C.** LSB Sample 190-1173A-47X-2, 132–134 cm, from a region of foliated breccia. Note that C is at a different scale than the other three photos and shows the slickensided surface. **D.** LSB Sample 190-1173A-69X-5, 78–85 cm, from near a healed fault, shows a subhorizontal interweaving CPO defined by dispersed, uniform clay particles.

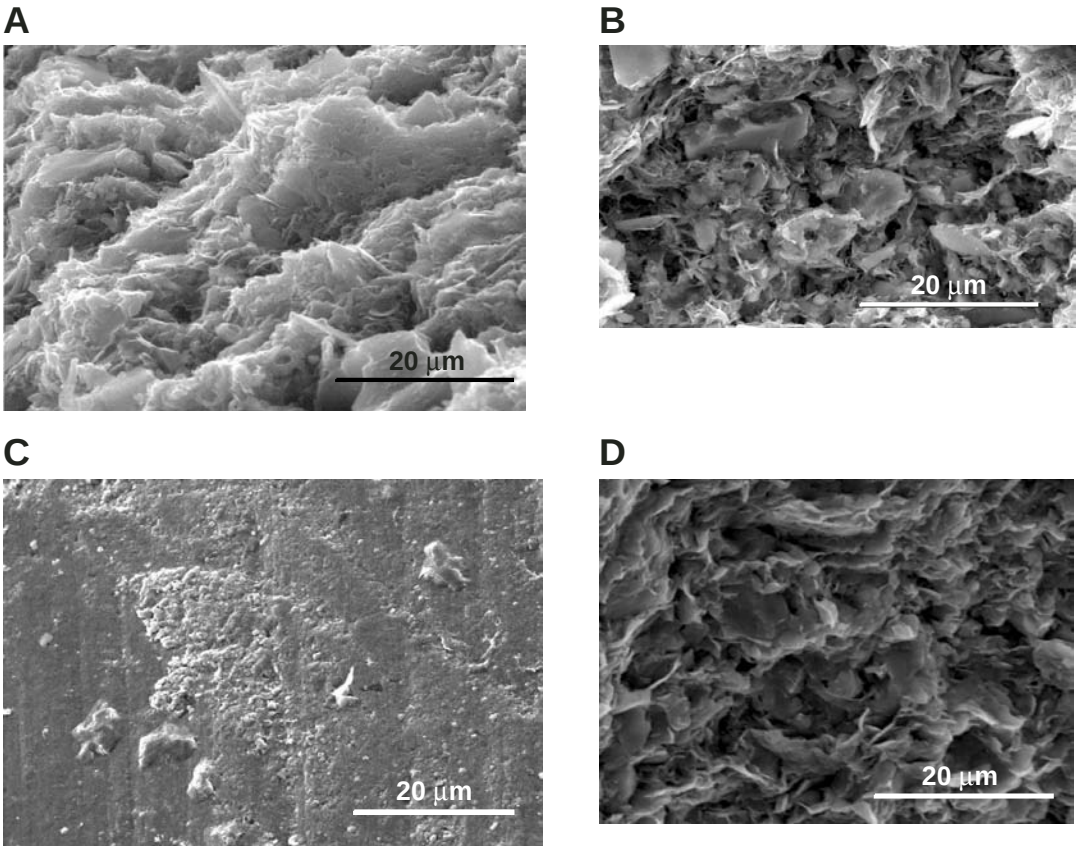

Figure F7. SEM photomicrographs of microstructural changes with depth at Site 1174. The photomicrograph scales are identical, and the up direction is toward the top of the page. **A.** OTW Sample 190-1174B-21R-2, 46–49 cm, displaying aligned particle stacks and domains of randomly oriented particles. **B.** USB Sample 190-1174B-37R-5, 64–68 cm. Note the variations in particle size and orientation. **C.** USB Sample 190-1174B-43R-5, 128–150 cm, has domains of inclined CPO, which are separated by regions with more open texture.

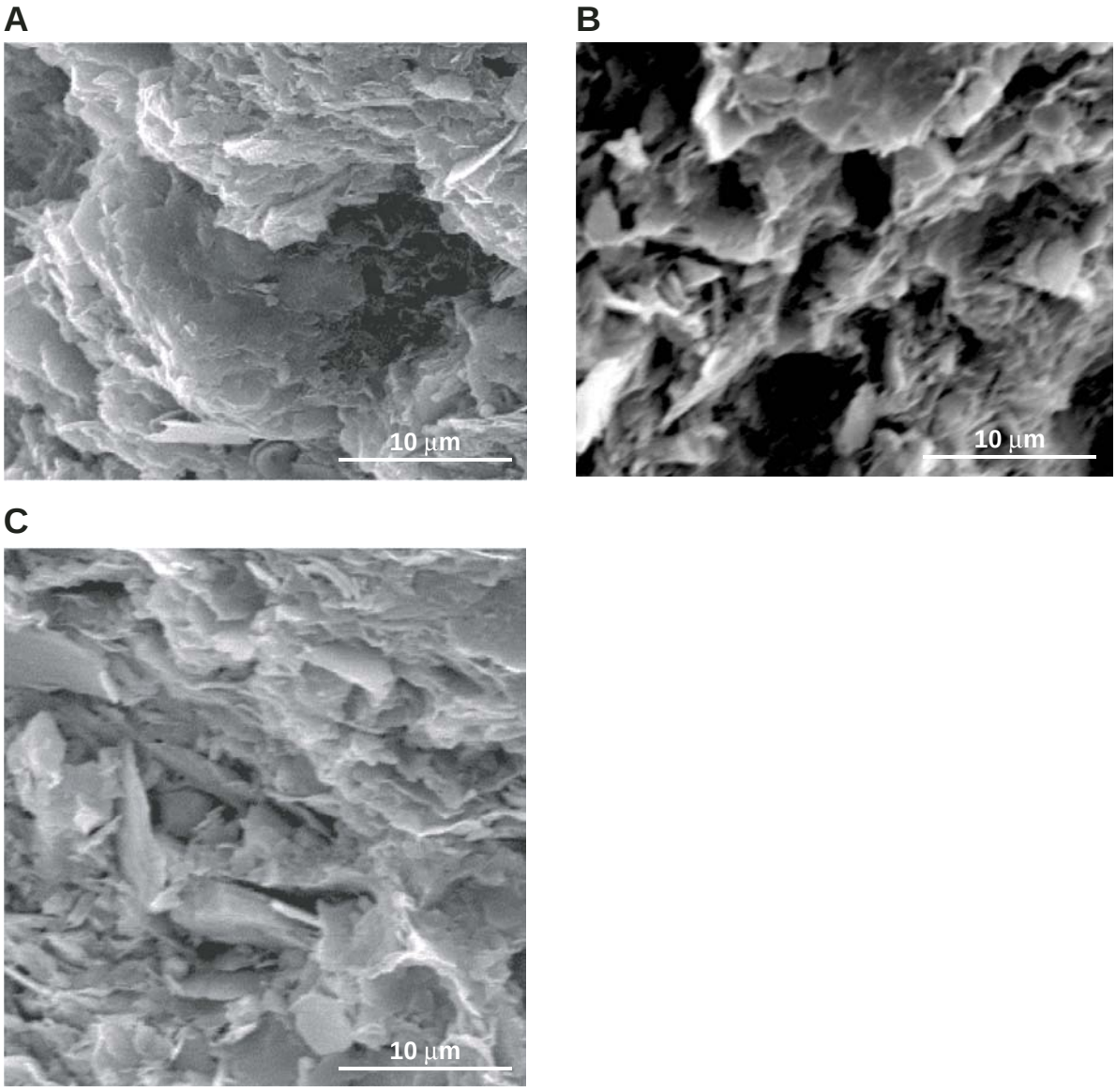

Figure F8. SEM photomicrographs of microstructural characteristics in the LSB at Site 1174. The photomicrograph scales are identical, and the up direction is toward the top of the page. **A.** Sample 190-1174B-58R-3, 11–15 cm, CPO. Note the smooth surfaces, edges, and the uniform shape and size of particles. **B.** Domainal microfabric of Sample 190-1174B-69R-7, 4–7 cm. **C.** Sample 190-1174B-85R-6, 64–69 cm, from below the décollement exhibits a penetrative CPO.

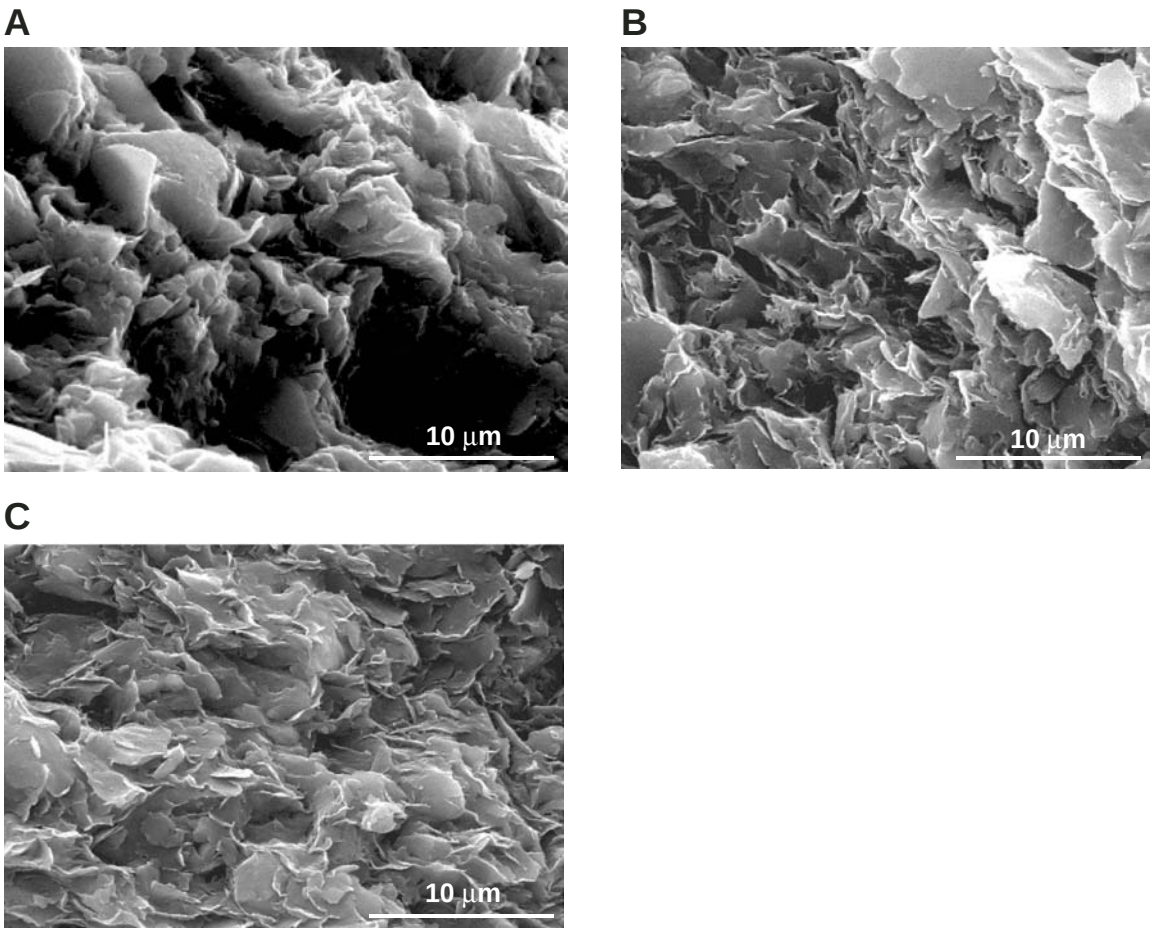

Figure F9. A, B. SEM photomicrographs of Sample 190-1174B-13R-2, 56–58 cm, collected adjacent to deformation bands in the ATW and displaying intersecting fabric planes. Photomicrograph B displays a higher-magnification view of the microstructure visible in A.

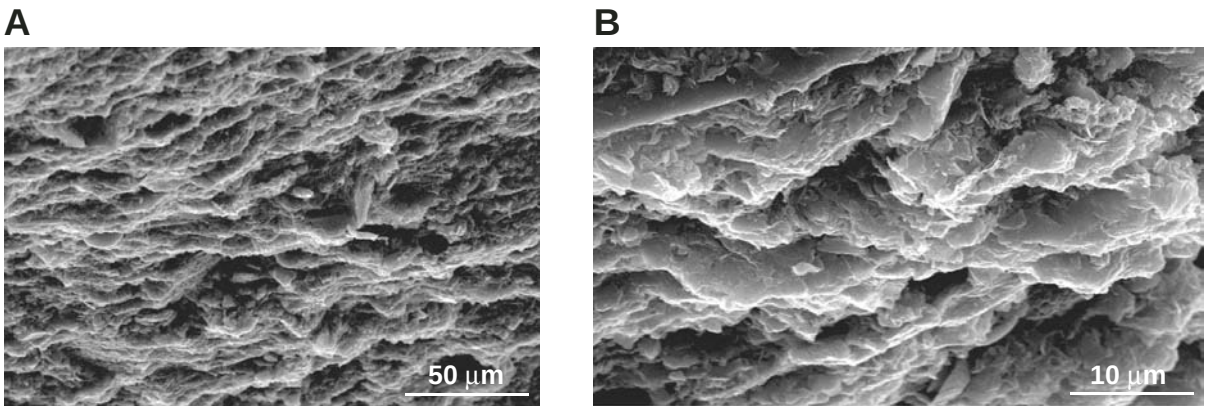

Figure F10. SEM photomicrographs of samples from the incipient thrust zone at Site 1174. **A.** Sample 190-1174B-35R-1, 52–53 cm, shows a well-developed CPO from a region away from a slip surface. **B.** Slickensided surface of Sample 190-1174B-35R-2, 84–87 cm.

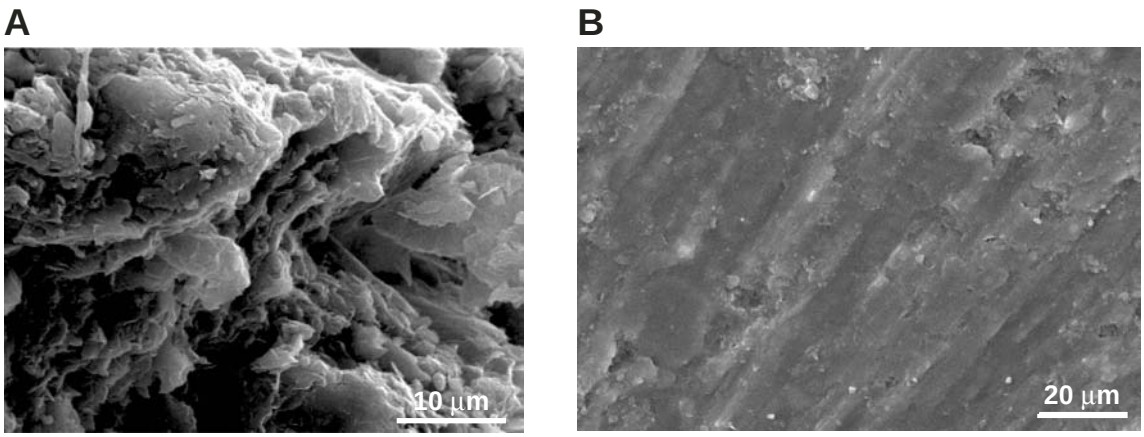

Figure F11. A, B. SEM photomicrographs of USB Sample 190-1174B-38R-6, 119–124 cm, illustrating incipient scaly fabric associated with fracture zones. Photomicrograph B is the same sample as shown in A but at a higher resolution. Note the intersecting fabric planes defined by stacked aggregates, which are oriented subhorizontally and dipping to the left side of view.

A

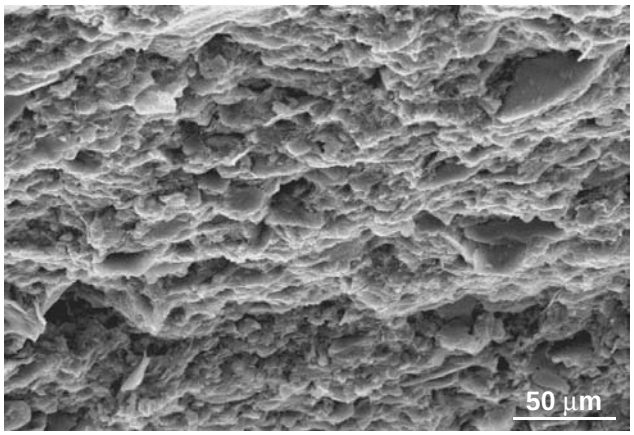

B

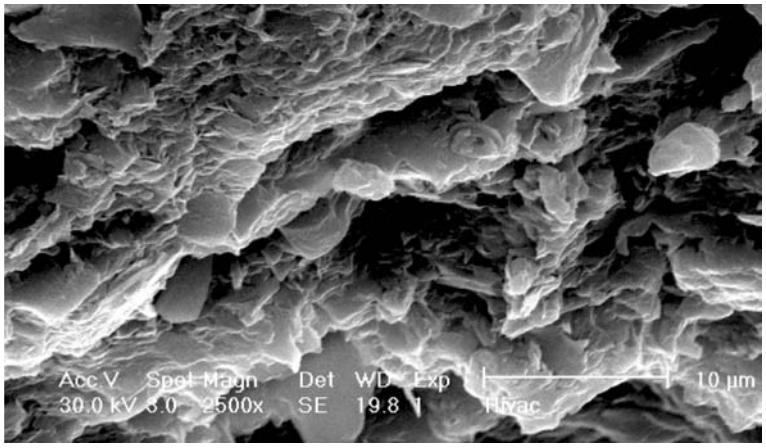

Figure F12. SEM photomicrographs of samples from deformed LSB sediments at Site 1174. **A.** Sample 190-1174B-66R-5, 32–36 cm, exhibits a slip surface with slickensides (bottom left) and a highly developed CPO (top right) associated with a fracture zone. **B–D.** SEM photomicrographs illustrating CPO development with depth in the décollement. The scale is the same in these three photomicrographs. **B.** Dense arrangement of particles in Sample 190-1174B-71R-2, 69–73 cm. **C.** Sample 190-1174B-71R-3, 69–72 cm, consists of domains of CPO and more open microfabrics. **D.** Penetrative CPO of Sample 190-1174B-73R-5, 53–55 cm.